

Monte-Carlo simulations of fast Newtonian and mildly relativistic shock breakout from a stellar wind

Hiroataka Ito^{1,2}, Amir Levinson³ and Ehud Nakar³

¹*Astrophysical Big Bang Laboratory, RIKEN, Saitama 351-0198, Japan; hirotaka.ito@riken.jp*

²*Interdisciplinary Theoretical & Mathematical Science Program (iTHEMS), RIKEN, Saitama 351-0198, Japan*

³*School of Physics & Astronomy, Tel Aviv University, Tel Aviv 69978, Israel; levinson@wise.tau.ac.il*

26 June 2020

ABSTRACT

Strong explosion of a compact star surrounded by a thick stellar wind drives a fast ($> 0.1c$) radiation mediated shock (RMS) that propagates in the wind, and ultimately breaks out gradually once photons start escaping from the shock transition layer. In exceptionally strong or aspherical explosions the shock velocity may even be relativistic. The properties of the breakout signal depend on the dynamics and structure of the shock during the breakout phase. Here we present, for the first time, spectra and lightcurves of the breakout emission of fast Newtonian and mildly relativistic shocks, that were calculated using self-consistent Monte-Carlo simulations of finite RMS with radiative losses. We find a strong dependence of the νF_ν peak on shock velocity, ranging from ~ 1 keV for $v_s/c = 0.1$ to ~ 100 keV for $v_s/c = 0.5$, with a shift to lower energies as losses increase. For all cases studied the spectrum below the peak exhibits a nearly flat component ($F_\nu \sim \nu^0$) that extends down to the break frequency below which absorption becomes important. This implies much bright optical/UV emission than hitherto expected. The computed lightcurves show a gradual rise over tens to hundreds of seconds for representative conditions. The application to SN 2008D/XRT 080109 and the detectability limits are also discussed. We predict a detection rate of about one per year with eROSITA.

Key words: shock breakout: general — shock waves — plasmas — radiation mechanisms: non-thermal — radiative transfer — scattering

1 INTRODUCTION

The collapse of a massive star creates a radiation dominated shock wave that propagates in the stellar envelope, breaks out, and ultimately emits the observed supernova light. In the majority of core-collapse events the breakout occurs at the edge of the stellar envelope, however, in stars that eject a sufficiently intense stellar wind prior to their collapse the RMS continues to propagate in the wind until reaching a large enough radius at which breakout ensues (Campana et al. 2006; Soderberg et al. 2008; Waxman et al. 2007; Katz, Budnik, & Waxman 2010; Balberg & Loeb 2011; Chevalier & Irwin 2011, 2012; Levinson & Nakar 2020). This is likely to occur in compact progenitors, like Wolf-Rayet stars, that exhibit broad emission lines, indicating fast winds with high mass flux. In particular, there is a growing body of evidence suggesting that many SN progenitors experience episodes of prodigious mass loss shortly (months to years) before core collapse, with rates as high as $\dot{M}_w \sim 10^{-3} - 10^{-1} M_\odot \text{ yr}^{-1}$ (Ofek et al. 2014b; Gal-Yam et al. 2014; Svirski & Nakar 2014). While more modest winds (with $\dot{M}_w \sim 10^{-7} - 10^{-4} M_\odot \text{ yr}^{-1}$) are commonly thought to be driven by radiative pressure, the nature of these intense eruptions is yet unclear (see discussion in, e.g., Shiode & Quataert 2014).

If the explosion energy is high enough and/or aspherical, the shock velocity may approach the speed of light, and in some circumstances may even be relativistic. An example is low luminosity GRBs that, in some scenarios (Nakar 2015), result from the breakout of a mildly or even highly relativistic shock from an extended envelope surrounding the compact progenitor. In general, a shock propagating at a velocity $v_s/c > \tau_{w*}^{-1} = 10^{-2} (R_{*11} v_{w3} / \kappa_{0.2} \dot{M}_{-3})$, where c is the speed of light, τ_{w*} is the total optical depth of the wind, $R_* = 10^{11} R_{*11}$ cm is the progenitor radius, $v_w = 10^3 v_{w3}$ km/s the wind velocity, $\dot{M}_w = 10^{-3} \dot{M}_{w-3}$ the mass loss rate and $\kappa = 0.2 \kappa_{0.2} \text{ gr}^{-1} \text{ cm}^2$ the Thomson opacity per unit mass, will remain radiation mediated upon transitioning into the stellar wind (Levinson & Nakar 2020). Fast Newtonian and mildly relativistic shocks, which are produced in powerful explosions of compact stars, likely surpass this criterion, hence their breakout is anticipated to occur gradually in the wind (as opposed to a sudden breakout from the stellar edge), at radii much larger than the stellar radius (see discussion in Section 5). The properties of the breakout signal in such shocks is the focus of this paper.

Observational evidence for shock breakout from a wind are rare and controversial. The leading candidate is probably the X-ray

flash from SN 2008D (Soderberg et al. 2008; Modjaz et al. 2009), for which the various properties of the emission suggest that the breakout occurred in a dense stellar wind rather than from the surface of the progenitor (e.g. Soderberg et al. 2008; Balberg & Loeb 2011; Svirski & Nakar 2014). Another type of SNe in which the emission is associated with a shock propagating in a wind are type II_n SNe, that show a bright and blue light curve and are thought to be powered by interaction. The rise time in these SNe has been attributed to a shock breakout emission (e.g., Ofek et al. 2010, 2014a). The last type of SNe that were suggested to be a breakout through a stellar wind are bright and very long ultra-luminous SNe where the mass of the wind is so large (several solar masses or more), that the breakout signal constitutes practically the entire main part of the SN light. The prototype of this class is SN2006gy (e.g., Chevalier & Irwin 2011).

During the gradual breakout from the wind the radiative losses continuously increase (Granot, Nakar & Levinson 2018; Levinson & Nakar 2020). These losses can significantly alter the shock structure and emission. For sufficiently slow shocks ($v_s/c \lesssim 0.05$) the radiation is in full thermodynamic equilibrium already inside the shock transition layer, and the emitted spectrum is a black body spectrum. In faster sub-relativistic shocks ($0.1 \lesssim v_s/c \lesssim 0.5$), termed fast Newtonian shocks, full thermodynamic equilibrium occurs only far downstream and the immediate downstream temperature depends sensitively on shock velocity (Katz, Budnik, & Waxman 2010; Levinson & Nakar 2020; Ito, Levinson & Nagataki 2020). In such shocks radiative losses can lead to notable effects. Analytic models that invoke the diffusion approximation (Ioka, Levinson & Nakar 2019) suggest that in fast Newtonian shocks the shock thickness and the immediate downstream temperature decrease with increasing losses during the breakout phase. However, what is the shape of the emitted spectrum and how it evolves with time is currently unknown. Moreover, as the shock velocity approaches $0.5c$ pair creation may become important, further complicating the problem. Computing the shape of the spectrum, which is particularly important for the estimation of detection limits at photon energies well below the X-ray peak (optical - UV in particular), is the main goal of this paper. Indeed, we show below that the flux in the optical-UV band is vastly higher (by several orders of magnitude) than that anticipated assuming a Wien spectrum.

The analysis outlined in this paper exploits a modified version of our Monte-Carlo code (Ito et al. 2018; Ito, Levinson & Nagataki 2020, hereafter ILN20) that incorporates photon escape, thereby enabling the calculations of the structure and spectrum of RMS during the breakout phase, when losses become substantial. The model tacitly assumes that the shock evolves in a quasi-steady manner, in the sense that it adjusts to the local conditions at any time such that a steady-state solution provides a good approximation to its structure and emission. The range of shock velocities considered here encompasses the fast Newtonian to mildly relativistic regimes, $0.1 \leq \beta_u \leq 0.5$, where β_u is the velocity of the upstream plasma in units of the speed of light, as measured in the shock frame. Fully relativistic RMS, that possess vastly different properties, will be considered in a follow up paper.

This paper is organized as follows. In Section 2 we describe the numerical method and the setup of our simulations. We present the computed structure of RMS in Section 3. The resulting spectrum of the photons escaping from RMS is shown in Section 4. Lightcurves computed by combining the simulations results with a realistic shock propagation model are presented in section 5. Applications to SN 2008D/XRT 080109 are discussed in section 6 and

detectability considerations in Section 7. We conclude in Section 8. Throughout the paper, the subscript u and d refer to the physical quantities at the far upstream and far downstream regions of the shock, respectively.

2 NUMERICAL SETUP

The details of the numerical method are described in Ito et al. (2018) and ILN20, where calculations of infinite shocks, i.e., shocks of sufficiently large optical depth that prevents any radiative losses, are presented. Here we extend the calculations to shocks of finite optical depth that allow photon escape from the upstream boundary of the shock.

In computing finite shock solutions, we employ two different methods, depending on whether a subshock forms or not. Our strategy to compute a smooth finite shock profile (that do not sustain a subshock) is to fix the downstream velocity β_d at a value lower than that obtained for an infinite shock with the same upstream conditions. For given downstream conditions, our code iteratively seeks a steady shock profile that conserves the energy-momentum flux throughout the flow, as in the case of an infinite shock (for further details, see Ito et al. 2018, ILN20). Since the compression ratio of the shock increases when radiative losses are present, this lower β_d leads to a solution with a larger energy escape. In any case, we first apply the above method to compute the finite shock structure. If the code fails to achieve convergence in this way, we introduce a subshock in the flow. In this alternative approach, we no longer fix the downstream velocity, instead the optical depth from the upstream boundary to the position of subshock, τ_{sub} , is fixed during the iteration. For the given optical depth τ_{sub} , our code again seeks a steady profile with a subshock.¹ In this case, a solution with larger energy escape can be obtained by reducing the value of τ_{sub} . Note that the downstream velocity β_d is obtained as an eigenvalue in this approach. In principle, it is possible to iteratively seek a solution with a subshock by fixing β_d and treating τ_{sub} as a free variable in the iterations. However, since extremely high spacial resolution is required around the subshock in order to accurately resolve the flow profile there, and since the position of the subshock is unknown a priori, it renders this technique far more challenging.

The radiative losses are quantified by the escape parameter f_{esc} which is the ratio of the energy flux carried by the escaping photons to the incoming energy flux of the baryons far upstream:

$$f_{\text{esc}} = -\frac{F_{\text{esc}}}{F_b}. \quad (1)$$

Here $F_{\text{esc}} < 0$ denotes the net energy flux of the photons at the upstream boundary of the simulation box² and $F_b = \Gamma_u(\Gamma_u - 1)n_u m_p \beta_u c^3$ is the energy flux of the baryons, where m_p is the proton rest mass and $\Gamma_u = (1 - \beta_u^2)^{-1/2}$ is the Lorentz factor of the upstream flow. Note that in our approach the value of f_{esc} is not an input parameter but rather an output of the calculations. A set of RMS solutions with different values of f_{esc} is obtained below by performing many simulations with different input values (β_d for smooth solutions and τ_{sub} when a subshock is present).

¹ As found in the case of infinite shocks (Ito et al. 2018, ILN20), the error in the energy-momentum conservation condition along the flow is reduced (converges within few percent) by introducing a subshock in the system when the code fails to find a smooth solution.

² F_{esc} is a negative quantity since we define positive energy flux in the direction along the flow.

In addition to β_d or τ_{sub} , the input parameters of the simulations are the velocity of the upstream flow, β_u , the proper baryon density at the far upstream region n_u , and the composition which we take to be purely hydrogen. As stated in the introduction, we are interested in exploring the regimes of fast Newtonian and mildly relativistic shocks. To that end we consider 3 models with different values of the upstream velocity, $\beta_u = 0.1, 0.25$ and 0.5 . As for the baryon density, we invoke a fixed value of $n_u = 10^{15} \text{ cm}^{-3}$ for the fiducial models which is identical to that adopted in the calculations of infinite shocks presented in ILN20. To explore the dependence on the density, we also compute a subset of RMS solutions with $n_u = 10^{12} \text{ cm}^{-3}$ for each β_u .

3 THE STRUCTURE OF RMS WITH ESCAPE

As shown in our previous study (ILN20), the properties of infinite RMS are vastly different in the sub-relativistic and the relativistic regimes. This holds true also for finite shocks. Below, we discuss the properties of finite sub-relativistic RMS ($\beta_u = 0.1$ and 0.25) and mildly relativistic RMS ($\beta_u = 0.5$) separately.

3.1 Sub-relativistic RMS

In Fig. 1, we plot the velocity profiles of infinite and finite fast Newtonian RMS ($\beta_u = 0.1$ and 0.25) as a function of the normalized optical depth, defined as $\hat{\tau} = \beta_u \int n \sigma_T dx$, for a wide range of escape fractions, up to $f_{\text{esc}} \sim 0.7$. For this range of f_{esc} , all solutions were found to have a smooth profile without a subshock. For an infinite shock, the width of the shock transition layer, l_{sh} is determined by the diffusion length of the photons ($\sigma_T n_u l_{sh} \approx 1/\beta_u$). Photon leakage is anticipated when the optical depth of the shock becomes smaller than this value. Consequently, as f_{esc} increases the shock width is expected to become narrower. This trend is clearly seen in Fig 1.

In Fig 1 we also plot the analytic RMS solutions (dotted lines) derived using the model outlined in Ioka, Levinson & Nakar (2019). These analytic solutions are characterized by a dimensionless free parameter that fixes the radiation pressure at the upstream boundary. It is given explicitly as:

$$\alpha = \frac{f_{\text{esc}}}{2p_{\text{esc}}}, \quad (2)$$

where $p_{\text{esc}} = P_{\text{esc}}/(\Gamma_u^2 n_u m_p \beta_u^2 c^2)$ is the momentum flux of the photons normalized by the baryon momentum flux at the upstream. For each of the analytic solutions depicted in Fig 1, we adopted an α value that was self-consistently determined from the simulation with same escape fraction. Interestingly, we find that for a given choice of β_u the value of alpha thereby obtained is independent of the escape fraction f_{esc} . For $\beta_u = 0.1$ (0.25), the finite shock simulations yield $\alpha = 14.2$ (5.6), with less than 1% deviation, for all the cases explored in the current study.

As already shown in our previous paper, there is excellent agreement between the numerical and analytical solutions of an infinite shock with $\beta_u = 0.1$. As for an infinite shock with $\beta_u = 0.25$, the analytic solution was also found to be in good agreement with the simulations, albeit with notable (though small) deviations owing to the larger inaccuracy of the diffusion approximation in this case. The finite shock solutions are also in good agreement with the simulations, with nearly perfect match for $\beta_u = 0.1$ and larger

deviations for $\beta_u = 0.25$. This confirms that the diffusion approximation is reasonable for fast Newtonian RMS even in the presence of large radiative losses.

Fig. 2 exhibits the corresponding temperature profiles. The sensitive dependence of the temperature on the upstream velocity seen in the figure is consistent with previous findings for infinite shocks (Weaver 1976; Katz, Budnik, & Waxman 2010, ILN20)³. The decline of the temperature with increasing losses (larger values of f_{esc}) is consistent with the trend found in Ioka, Levinson & Nakar (2019). The reason for this behaviour is that larger losses give rise to a higher compression ratio (i.e., a smaller downstream velocity) and, consequently, a larger diffusion length behind the shock which, in turn, enhances photon production in the immediate downstream. Our simulations confirm that the decline in temperature during a gradual breakout is a robust feature.

3.2 Mildly relativistic RMS

The velocity profiles of RMS with $\beta_u = 0.5$ and different escape fractions are displayed in Fig. 3. In this regime the diffusion approximation adopted in Ioka, Levinson & Nakar (2019) is totally inapplicable, hence analytic solutions cannot be obtained. Moreover, the shock opacity is dominated by newly created pairs (Fig. 4.) and, therefore, the solutions are given as functions of the normalized pair loaded optical depth, $\tau_* = \beta_u \int \Gamma(n + n_{\pm}) \sigma_T dx$.

As in the previous cases, the shock transition layer becomes narrower as the escape fraction increases. On the other hand, unlike the previous cases, solutions with sufficient losses (more than a few percents) exhibit a subshock. As seen in the figure, the strength of the subshock increases with increasing f_{esc} , becoming quite large as f_{esc} approaches 0.5.

The profiles of the temperature and pair-loading parameter (pair-to-baryon ratio) are shown in Fig. 4. As seen, unlike in fast Newtonian shocks, the immediate downstream temperature in this case is practically independent of f_{esc} . This is a consequence of temperature regulation by exponential pair creation (for a detailed explanation of this effect see Levinson & Nakar 2020, and references therein). The spikes seen in the temperature curves correspond to overheated plasma immediately behind the subshock. Since the subshock is collisionless, heating of the plasma occurs on kinetic scales which are vanishingly small. The width of the spike is thus determined by the cooling length of the overheated plasma, which is much smaller than the photon mean free path, as explained in detail in Ito et al. (2018).

3.3 Dependence of shock structure on the upstream density

In all the above solutions the upstream baryon density was taken to be $n_u = 10^{15} \text{ cm}^{-3}$. This particular value was chosen in order to compare the finite shock solutions with the simulations of infinite shocks performed by ILN20. However, in most cases of shock breakout from a stellar wind the typical density is expected to lie in the range $n_u \sim 10^{12} - 10^{13} \text{ cm}^{-3}$. While the velocity profile as a function of optical depth is independent of n_u , the temperature (as well as the pair density for $\beta_u = 0.5$) and the photon spectrum do

³ From the current simulations we find that the temperature roughly scales as $T \propto \beta^{3.4}$ in the range $0.1 \leq \beta_u \leq 0.25$. This is slightly steeper than the dependence $T \propto \beta_u^3$ found in ILN20 in the range $0.1 \leq \beta_u \leq 0.5$, since the regulation of temperature by the vigorous pair production is already important at $\beta_u = 0.5$.

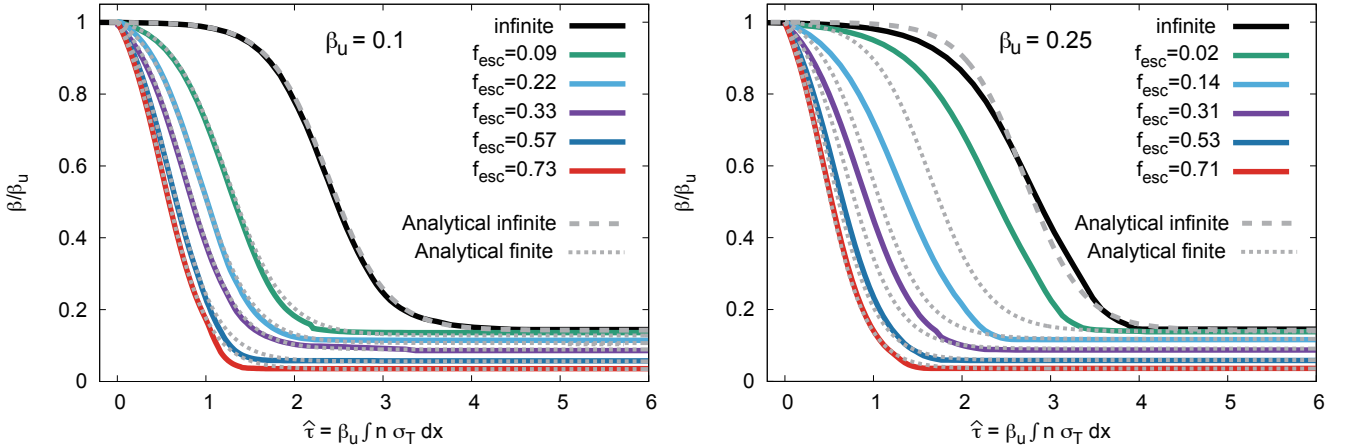


Figure 1. Velocity profiles of RMS with upstream velocities $\beta_u = 0.1$ (left) and $\beta_u = 0.25$ (right), plotted as functions of the normalized optical depth $\hat{\tau} = \beta_u \int n \sigma_T dx$. The solid black line in each panel displays the simulation result for the infinite shock, while the green, cyan, magenta, blue and red lines depict the results for finite shocks with downstream velocities $\beta_d/\beta_{d,inf} = 0.95, 0.8, 0.6, 0.4$ and 0.25 , respectively, where $\beta_{d,inf}$ denotes the downstream velocity of the infinite shock ($f_{esc} = 0$). The resulting escape fraction obtained in each simulations is indicated in the figure legends. The grey dashed line marks the analytical infinite shock solution and the grey dotted lines are the corresponding analytical finite shock solutions obtained for the values of f_{esc} and α found in the simulations. The values of α used for the fits are 14.2 and 5.6 for $\beta_u = 0.1$ and 0.25, respectively, independent of f_{esc} .

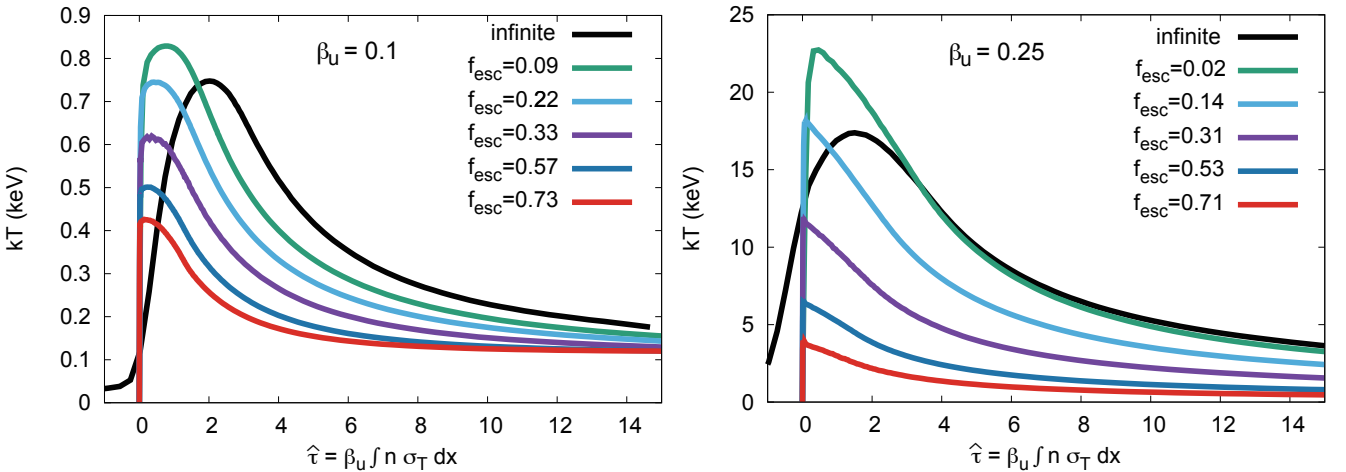


Figure 2. Temperature profiles obtained for the solutions in Fig. 1. Note that the extent of the horizontal axis is larger than in Fig. 1.

have certain dependences on the number density. To elucidate the dependence of RMS properties on the upstream baryon density we performed additional simulations of finite and infinite shocks with $n_u = 10^{12} \text{ cm}^{-3}$.

In Fig. 5 we compare temperature profiles of sub-relativistic shocks ($\beta_u = 0.1$ and 0.25) obtained for $n_u = 10^{15} \text{ cm}^{-3}$ and $n_u = 10^{12} \text{ cm}^{-3}$. As seen, a lower density gives rise to a lower temperature, although the dependence is rather weak (a factor of 2 change over three decades in density). This, nonetheless, has important impact on the spectral luminosity at frequencies below the peak, as will be discussed in section 5. The results exhibited in Fig. 5 are in very good agreement with analytic estimates (Ioka, Levinson & Nakar 2019; Levinson & Nakar 2020). A similar comparison for the $\beta_u = 0.5$ shock is exhibited in Fig. 6, and it is seen that in this case the temperature is practically independent of density, whereas the dependence of the pair content is very

weak. This is a consequence of the pair creation thermostat discussed above.

4 THE SPECTRUM OF ESCAPING RADIATION

In Fig. 7, we show the spectral energy distribution of photons escaping through the upstream boundary of the simulation box, $f_\nu = -\frac{df_{esc}}{d\nu}$, for each model. Each line, computed for a particular value of f_{esc} , as indicated in the figure, represents the instantaneous spectrum emitted during a gradual shock breakout from a wind-like medium at the radius at which the optical depth to infinity ahead of the shock roughly equals the local shock width (smaller f_{esc} values correspond to earlier emission). However, the overall normalization of the spectra does not take into account the full evolution of the shock and the structure of the ejecta. Lightcurves computed by combining the simulations results with a realistic shock propagation model are presented in section 5. It is emphasized that our re-

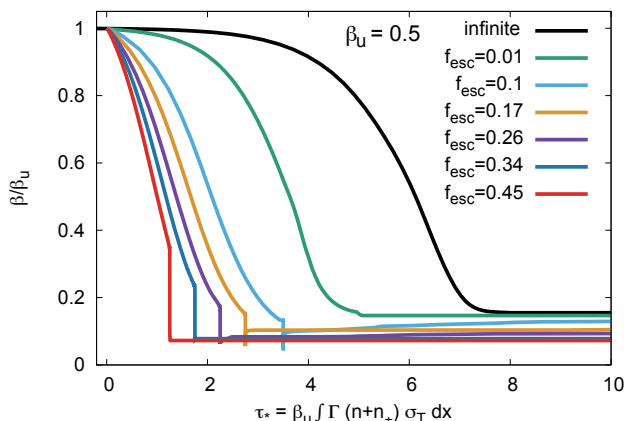


Figure 3. Velocity profiles of RMS with an upstream velocity $\beta_u = 0.5$, plotted as functions of the normalized pair-loaded optical depth $\tau_* = \beta_u \int \Gamma(n+n_{\pm})\sigma_T dx$. The profiles depicted by the solid black (infinite shock) and green lines are found to be smooth (contain no subshock). The cyan, brown, magenta, blue and red lines show the simulation results for finite shocks that contain a subshock. The resulting escape fractions are given in the figure legends.

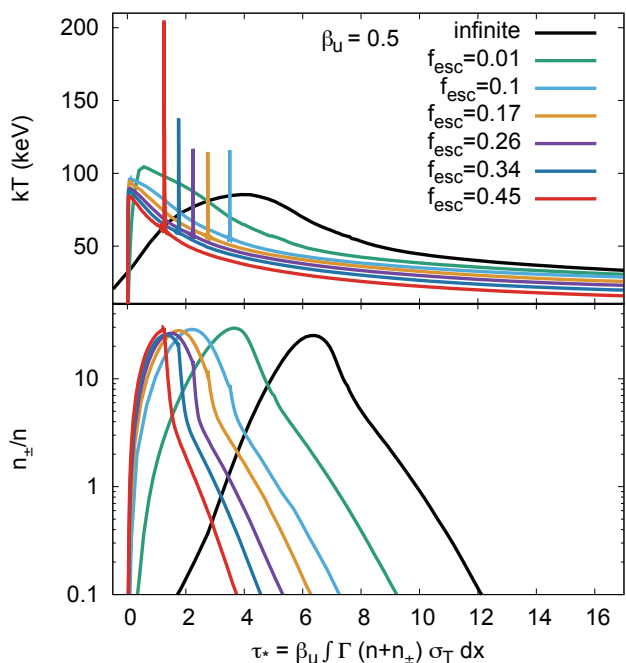


Figure 4. Profiles of temperature (*top*) and pair-to-baryon ratio (*bottom*) obtained for the solutions shown in Fig. 3. Note the larger extent of the horizontal axis.

sults provide, for the first time, spectra of shock breakout emission in a wind from self-consistent simulations.

In all cases exhibited in Fig. 7, the spectral peak energy reflects the immediate downstream temperature, that is, $E_p \sim 3kT_d$. The spectral softening (i.e., the shift of E_p to lower energies) during the rise of the luminosity seen in the Newtonian shocks is a consequence of the decline of the downstream temperature (see Fig. 2). For a shock with $\beta_u = 0.1$ (0.25), the spectral peak evolves in the soft, $E_p \sim 1\text{keV}$ (hard, $E_p \sim 10\text{keV}$), X-ray band. As discussed in Ioka, Levinson & Nakar (2019), the superposition of emission

during the hard-to-soft evolution may account for the time integrated, non-thermal spectrum observed in the shock breakout candidate XRT080109 (Soderberg et al. 2008). In contrast to the fast Newtonian shocks, the mildly relativistic ($\beta_u = 0.5$) shock shows no softening, with E_p maintained around $\sim 200\text{keV}$ during the luminosity rise. This is again a consequence of the pair thermostat mentioned in the previous section.

A notable feature common to all spectra is the sudden change in slope below the peak. While the portion of the spectrum around the peak (the bump) has a Wien shape ($I_\nu \propto \nu^3 \exp(-h\nu/kT)$)⁴, the soft tail below the peak has a spectral slope close to that of free-free emission, $I_\nu \propto \nu^0$, extending down to the break frequency below which the free-free absorption is fast enough to establish a full thermodynamic equilibrium (and the spectrum hardens to a black body slope). As discussed in ILN20, the existence of a substantial soft tail implies that the breakout signal well below the spectral peak should be much brighter (by orders of magnitude) than that naively expected by invoking a Wien spectrum in the entire spectral range. This has important implications for detection limits in optical/UV band and the interpretation of shock breakout signals (see section 5 for detailed calculations).

Regarding the spectral portion above the peak, we find no notable deviations from a Wien spectrum. Hence, an exponential cut-off at high energies is likely to be a robust feature of (planar) fast Newtonian and, perhaps, mildly relativistic shocks at breakout. Note, however, that following the breakout episode the shock transforms into a collisionless shock that keeps propagating in the optically thick medium; during this phase a power-law spectrum is expected, as discussed in Svirski & Nakar (2014). The results of our simulations indicate that, contrary to previous claims (Wang, et al. 2007; Suzuki & Shigezuma 2010), bulk Comptonization is unlikely to be the origin of the high energy, non-thermal tail observed in XRT080109. It is worth noting that for the $\beta_u = 0.5$ shock, slight hardening of the spectrum may occur when the losses exceed the values explored here ($f_{esc} = 0.45$). Such deviations are indeed indicated by preliminary calculations with larger escape fractions. However, we find that when $f_{esc} > 0.45$, the subshock becomes exceedingly strong and intermittent, and the simulation does not converge to a steady-state solution.⁵ This might suggest that the transition to the collisionless regime becomes fully dynamic, likely involving turbulence and other stochastic effects. In this regard it is worth pointing out that the strong subshock may give rise to efficient particle acceleration. Once the energy dissipated in the subshock amounts to a considerable fraction of the total shock energy, Compton scattering and synchrotron emission by the accelerated pairs may significantly modify the high-energy portion of the spectrum, conceivably giving rise to a nonthermal gamma-ray flash. We defer the exploration of such effects to a future work.

4.1 Dependence of spectrum on the upstream density

A comparison of spectra obtained for shocks with upstream densities $n_u = 10^{15}\text{cm}^{-3}$ and $n_u = 10^{12}\text{cm}^{-3}$ is given in Fig. 8. As

⁴ This bump is more prominent in faster shocks, for which the departure from thermodynamic equilibrium is larger. For the cases studied here we find that the Wien spectrum provides a good fit for the entire bump only for $\beta_u = 0.25$ and 0.5 . For $\beta_u = 0.1$ it can only fit the spectral portion above the peak ($h\nu \gtrsim E_p$).

⁵ To be concrete, for any number of iterations, the simulation cannot find a steady profile which satisfies energy-momentum conservation to within an error of a few %.

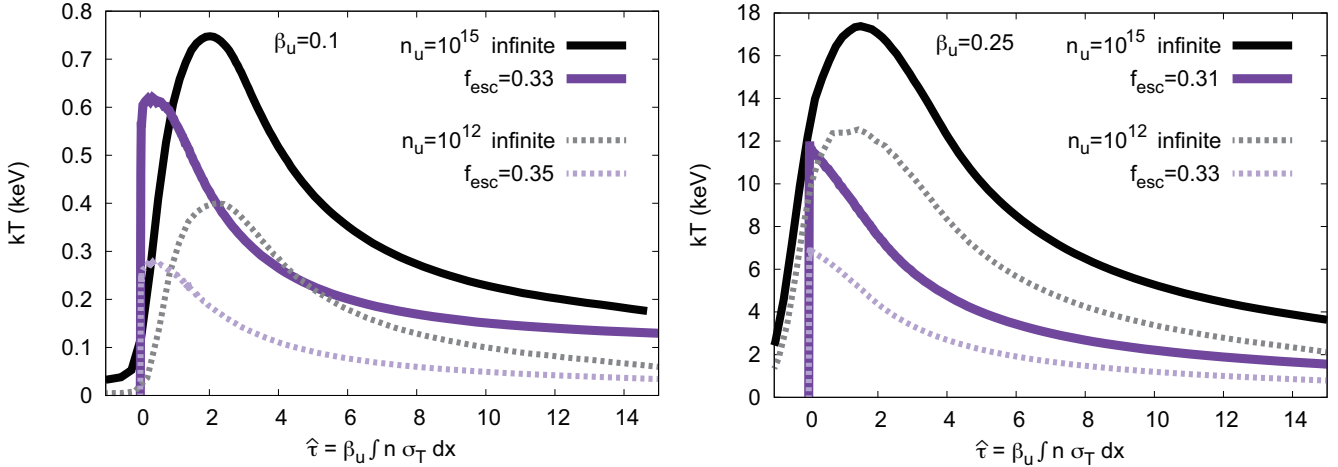


Figure 5. The temperature profile for the simulations with upstream density of $n_u = 10^{15} \text{ cm}^{-3}$ (solid lines) and 10^{12} cm^{-3} (dotted lines). The left and right panels display the results for $\beta_u = 0.1$ and 0.25 , respectively. The black and magenta lines show the cases of the infinite and finite shocks for $\beta_d = 0.6\beta_{d,\text{inf}}$, respectively. Note that the slight difference found in the escape fraction of finite shocks for different n_u is due to the numerical errors.

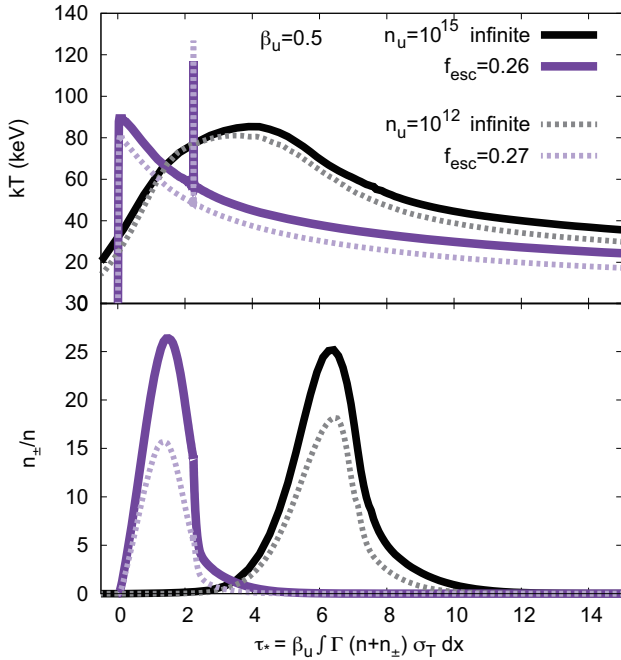


Figure 6. The temperature (top) and pair-to-baryon ratio (bottom) profiles for the simulations with upstream density of $n_u = 10^{15} \text{ cm}^{-3}$ (solid lines) and 10^{12} cm^{-3} (dotted lines). The black and magenta lines show the cases of the infinite and finite shocks for $\tau_{\text{sub}} = 2.25$, respectively. Note that the slight difference found in the escape fraction of finite shocks for different n_u is due to the numerical errors.

seen, the main effect is a shift of the spectrum to lower energies as the upstream density decreases, with a little change in the overall spectral shape. This behaviour stems from the dependence of the downstream temperature on density (see Figs. 5 and 6). The shift is smaller the larger the shock velocity is, and is practically absent in the $\beta_u = 0.5$ case.

An important consequence of this dependence is that the relative brightness of emission below the peak increases substantially with decreasing density (in other words, the ratio between the bolo-

metric luminosity and the luminosity emitted in some band below the peak decreases with decreasing density). For example, for $\beta_u = 0.1$ (0.25) the ratio between the luminosity at the peak and the optical luminosity (at $\sim 1 \text{ eV}$) decreases by a factor of about 10 (5) as the density decreases from $n_u = 10^{15} \text{ cm}^{-3}$ to $n_u = 10^{12} \text{ cm}^{-3}$. Hence, shock breakout in a lower density environment is preferential for the detection of the optical/UV source.

Another effect caused by the change in density is found in the break frequency below which free-free absorption becomes important. Since the photon density is much lower in the lower density simulation, the break occurs at a lower frequency. Note that the large contrast in the photon number density is not apparent from the figure, since the displayed spectrum is normalized by the baryon energy flux F_b .

5 LIGHT CURVE OF SPHERICAL SHOCK BREAKOUT FROM A STELLAR WIND

In this section we present approximate calculations of shock breakout lightcurves at different bands by combining the results of the previous section with a model for blast wave propagation in a wind.

The dynamics of the shock, and in particular the energy deposition profile, depend on the properties of the ejecta, that should be given as input for the calculations of the shock evolution in the wind. A common choice is the self-similar solution of Sakurai (1960) that provides a good approximation for the structure of the shocked layer near the edge of the envelope of the progenitor following the passage of shock. The energy profile within the ejecta, obtained from the Sakurai (1960) solution, can be expressed in terms of the ejecta velocity, v , as:

$$E(v) = E_0(v/v_0)^{-\lambda} = \frac{4\pi c v_0}{\kappa} R_*^2 (v/v_0)^\lambda, \quad (3)$$

where v_0 and $E_0 = 4\pi c v_0 R_*^2 / \kappa$ are, respectively, the velocity and energy of the front shell of optical thickness c/v_0 (Nakar & Sari 2010), and κ denotes the opacity of the stellar envelope. The index λ depends on the power-law index n_* of the envelope density profile near the edge as: $\lambda = (1 + 0.62n_*)/0.19n_*$. For typical envelopes $n_* = 1 - 3$, wherein $n_* \approx 1.5$ for convective envelopes and $n_* \approx 3$

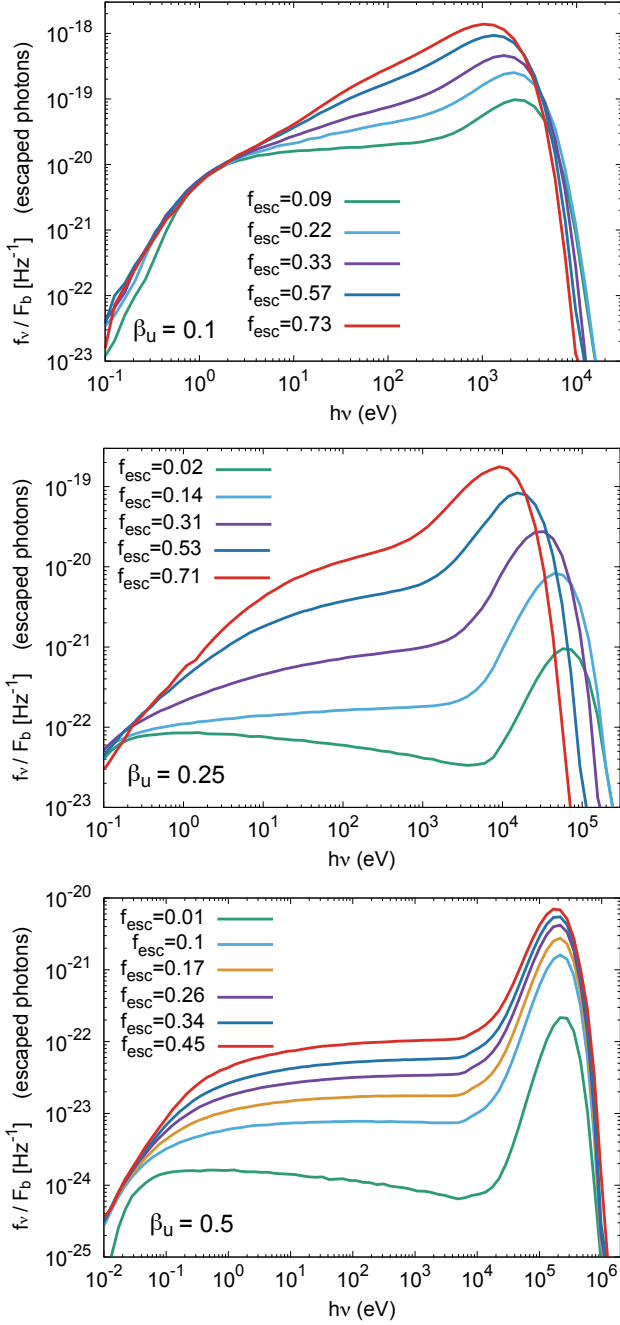


Figure 7. Shock-frame, flux density of escaping photons, $f_v = -\frac{dF_{esc}}{dv}$, normalized by the total kinetic energy flux of baryons at the upstream boundary, $F_b = \Gamma_u(\Gamma_u - 1)n_u m_p c^3 \beta_u$. The top, middle and bottom panels display the results for shock velocities $\beta_u = 0.1, 0.25$ and 0.5 , respectively. The different lines in each panel correspond to different values of the escape fraction, as indicated.

for radiative envelopes. Henceforth, we choose $n_* = 3$ and $\kappa = 0.2 \text{ cm}^2 \text{ g}^{-1}$, which is suitable for Wolf-Rayet stars. With this choice (Nakar & Sari 2010) $\lambda = 5$,

$$E_0 \approx 1.6 \times 10^{44} \text{ erg} \left(\frac{E_{exp}}{10^{51} \text{ erg}} \right)^{0.58} \left(\frac{M_*}{5M_\odot} \right)^{-0.41} \left(\frac{R_*}{10^{11} \text{ cm}} \right)^{1.66}, \quad (4)$$

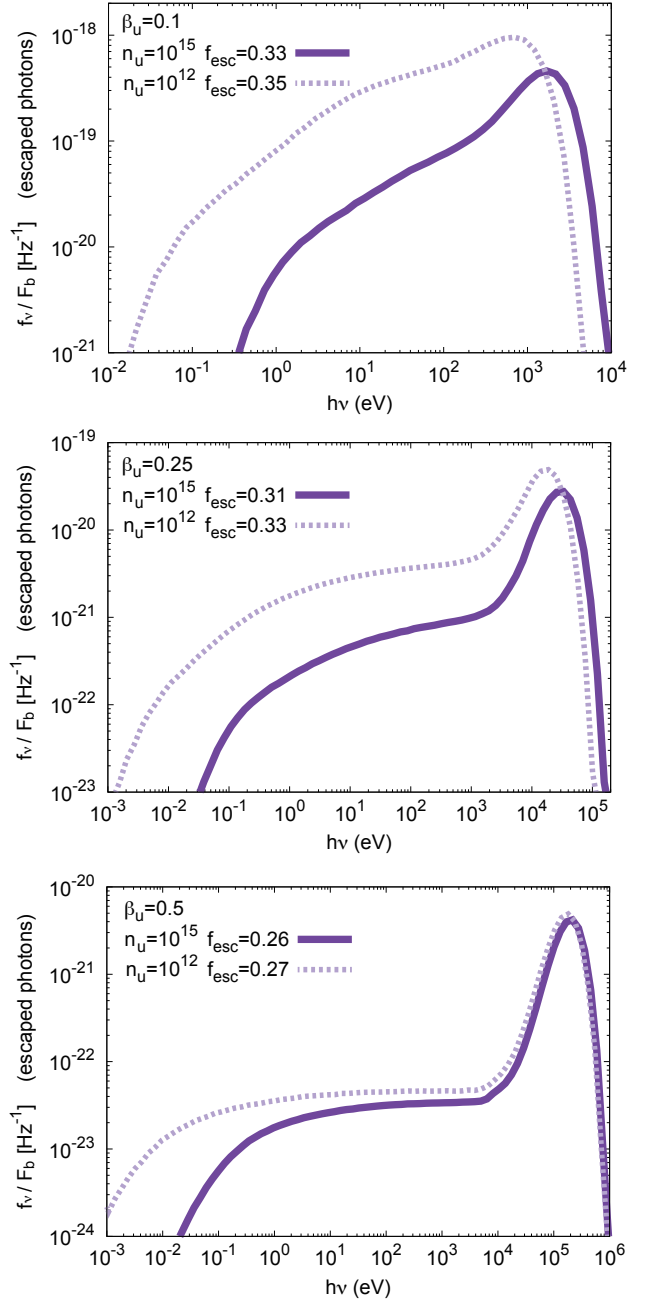


Figure 8. Same as Fig. 7, but for comparison between $n_u = 10^{15} \text{ cm}^{-3}$ (solid lines) and $n_u = 10^{12} \text{ cm}^{-3}$ (dotted lines) at a nearly identical escape fraction.

and

$$v_0 \approx 0.3c \left(\frac{E_{exp}}{10^{51} \text{ erg}} \right)^{0.58} \left(\frac{M_*}{5M_\odot} \right)^{-0.41} \left(\frac{R_*}{10^{11} \text{ cm}} \right)^{-0.33}, \quad (5)$$

where E_{exp} and M_* denote the explosion energy and the mass of the ejecta, respectively.

In cases where the progenitor is surrounded by an optically thick wind ($\tau_w > c/v_0$), the shock driven into the wind by the expanding ejecta remains radiation mediated. The subsequent shock dynamics is dictated by the density profile of the wind. We shall invoke a spherical wind with a density profile $\rho_w \propto r^{-2}$. The total mass swept up by the shock as it reaches a radius r_s is

$m_s = \int_{R_*}^{r_s} 4\pi r^2 \rho_w dr \approx (4\pi\tau_w R_* / \kappa_w) r_s$, where κ_w is the opacity of the wind, henceforth assume to be equal to the envelope opacity, $\kappa_w = \kappa$, and the swept up energy is $E_s = m_s v_s^2$, where v_s is the shock velocity at r_s . Equating E_s with the energy injected into the shock by the ejecta, $E(v_s)$, yields $v_s(r_s) = v_0 (cR_*/v_0\tau_w r_s)^{1/(4+2)}$. We find it convenient to express the result in terms of the local optical depth, $\tau_s = \tau_w(R_*/r_s)$, rather than r_s . Using $\lambda = 5$ and Eqs. (4), (5) we obtain

$$E_s \approx 1.7 \times 10^{45} \text{ erg} \left(\frac{E_{exp}}{10^{51} \text{ erg}} \right) \left(\frac{M_*}{5M_\odot} \right)^{-0.72} \left(\frac{R_*}{10^{11} \text{ cm}} \right)^{1.4} \times \left(\frac{\tau_w}{30} \right)^{1.4} \left(\frac{\tau_s}{10} \right)^{-0.72}, \quad (6)$$

$$v_s \approx 0.18c \left(\frac{E_{exp}}{10^{51} \text{ erg}} \right)^{0.5} \left(\frac{M_*}{5M_\odot} \right)^{-0.36} \left(\frac{R_*}{10^{11} \text{ cm}} \right)^{-0.29} \times \left(\frac{\tau_w}{30} \right)^{-0.29} \left(\frac{\tau_s}{10} \right)^{0.14}. \quad (7)$$

Note the very weak dependence of v_s on τ_s . The dynamical time can be expressed as

$$t = r_s/v_s \approx 55 \text{ s} \left(\frac{E_{exp}}{10^{51} \text{ erg}} \right)^{-0.5} \left(\frac{M_*}{5M_\odot} \right)^{0.36} \left(\frac{R_*}{10^{11} \text{ cm}} \right)^{1.29} \times \left(\frac{\tau_w}{30} \right)^{1.29} \left(\frac{\tau_s}{10} \right)^{-1.14}. \quad (8)$$

A rough estimate of the breakout density, $\rho_b = \rho_w(r_b)$, where r_b denotes the shock radius at breakout, can be obtained as follows: first we express the wind density in terms of the optical depth as $\rho_w(\tau_s) = \tau_s^2 / (\kappa\tau_w R_*)$. We then substitute the optical depth at the breakout radius, $\tau_s(r_b) = c/v_b(1 + f_\pm)^{-1}$, into the latter expression, where $v_b = v_s(r_b)$ and the factor f_\pm denotes the pair-to-baryon ratio at the shock which is only relevant for $\beta_u = 0.5$. This yields

$$\rho_b \approx 1.5 \times 10^{-10} \left(\frac{v_b}{0.1c} \right)^{-2} \left(\frac{\tau_w}{30} \right)^{-1} \left(\frac{R_*}{10^{11} \text{ cm}} \right)^{-1} (1 + f_\pm)^{-2} \text{ gr cm}^{-3}. \quad (9)$$

It is seen that the number density in the breakout zone lies in the range $10^{11} - 10^{14} \text{ cm}^{-3}$ for anticipated conditions. Note the scaling $v_b \propto \rho_b^{0.51} E_{exp}^{0.9} M_*^{-0.64}$, $E_s \propto \rho_b^{-1.65} E_{exp}^{-0.15} M_*^{0.1}$.

We now use the above results in conjunction with the simulations to compute lightcurves in different bands. We adopt the following procedure: First, we ignore, for simplicity, the dependence of the shock velocity on τ_s and take it to be constant during the breakout phase, which is justified by virtue of the very weak dependence in Eq. (5). For each RMS case simulated we choose a set of values for E_{exp} , M_* , R_* and τ_w , for which v_s in Eq. (5) equals the simulated shock velocity (i.e., $\beta_u = v_s/c = 0.1, 0.25$ or 0.5), as indicated in the titles of figures 9-11. Next, we identify τ_s with the shock width, specifically, the pair-unloaded optical depth of the shock, $\tau_s = \int_0^{l_s} n\sigma_T dx$, measured in the simulations from the upstream boundary at $\tau = 0$ to the downstream point l_s where $\beta = \beta_u/6.5$. For each value of τ_s we then obtain the escape fraction f_{esc} from the analysis in section 3 (see Figs. 1 and 3), and the shock energy and expansion time from Eqs. (6) and (8). The bolometric luminosity of the breakout emission at time t is then given by $L_{bol} = f_{esc} L_s$, where $L_s = E_s/t$ denotes the mean change in shock energy with time. The spectral luminosity is given in terms of the flux density f_ν shown in Fig. (7) as $L_\nu = f_\nu(L_s/F_b)$. Note that $\int_0^\infty f_\nu d\nu = f_{esc} F_b$, so that $\int_0^\infty L_\nu d\nu = f_{esc} L_s = L_{bol}$, as required.

We note that for a given velocity $\beta_u = v_b/c$, once a value of the product $\tau_w R_*$ is chosen the breakout density is fixed by Eq. (9). This means that the upstream density invoked in our simulations is

inconsistent with the breakout density. While the bolometric luminosity is independent of the density, the spectral luminosity below the peak does depend on it. Performing additional simulations with different densities is highly demanding. As a compromise we exhibit below lightcurves computed for the densities $n_u = 10^{15} \text{ cm}^{-3}$ and 10^{12} cm^{-3} employed in the simulations presented in the preceding sections. For the choice of parameters in 9-11 Eq. (9) yields a breakout density of 3×10^{13} , 1.5×10^{13} and $1.2 \times 10^{11} \text{ cm}^{-3}$ for $\beta_u = 0.1, 0.25$ and 0.5 , respectively. Note that $f_\pm \sim 10$ is employed for $\beta_u = 0.5$ (see Fig. 4). In practice the density will decline during the gradual breakout by up to a factor of a few.

In each of the figures 9-11 we show 3 sets of light curves computed for the choice of model parameters indicated in each figure title, which are suitable for Wolf-Rayet stars surrounded by optically thick wind, that upon exploding release energy in the range $E_{exp} = 10^{51} - 10^{52} \text{ erg}$. From top to bottom, the panels in each figures show the bolometric, X-ray ($h\nu = 0.3 - 10 \text{ keV}$), NUV ($\lambda_{ph} = 250 \text{ nm}$) and optical ($\lambda_{ph} = 650 \text{ nm}$) light curves, where λ_{ph} is the wavelength of photons. In addition to the light curves produced based on the fiducial simulations ($n_u = 10^{15} \text{ cm}^{-3}$), we also plot the estimates for $n_u = 10^{12} \text{ cm}^{-3}$. Here we assume that the flux ratio at a given energy does not vary largely with the escape fraction, and the estimates are made by multiplying the fiducial light curves by a constant factor determined by the flux ratio between the simulations for $n_u = 10^{15} \text{ cm}^{-3}$ and $n_u = 10^{12} \text{ cm}^{-3}$ shown in Fig. 8. Given our estimates of breakout density, realistic light curves are expected to lie between the two shown for $\beta_u = 0.1$ and $\beta_u = 0.25$ but closer to the upper curve (for $n_u = 10^{12}$), while $\beta_u = 0.5$ is expected to be slightly above the two curves. Note that $L_s = E_s/t \propto E_{exp}^{1.5} M_*^{-1.1} (\tau_w R_*)^{0.1}$ depends very weakly on the wind's opacity. Substantially larger luminosities require larger explosion energies and smaller ejecta mass.

As seen in the figure, while the energy deposition rate L_s declines with time, the emission becomes brighter as the escape fraction increases. Since the escape fraction at the latest time is large ($f_{esc} \gtrsim 0.5$), the light curves are expected to reach the peak soon after and connect to cooling envelope emission. The bolometric luminosity represents the emission at X-ray and gamma-rays: $\sim \text{keV}$ for $\beta_u = 0.1$, $\sim 10 \text{ keV}$ for $\beta_u = 0.25$ and $\sim 100 \text{ keV}$ for $\beta_u = 0.5$. Although the optical/UV are much dimmer, it is much brighter than the naive expectation from Wien spectra as mentioned in the previous section.

6 COMPARISON TO SN 2008D/XRT 080109

The leading candidate of a SN shock breakout from a dense stellar wind is SN2008D/XRT 080109 (Soderberg et al. 2008; Modjaz et al. 2009). The X-ray flash seen in this SN has a rise time of 50 – 100 s, followed by a shallow power-law decay that lasts for about 300 s. The peak luminosity is $\sim 4 \times 10^{43} \text{ erg/s}$ and the time integrated spectrum over the entire observed emission, which is dominated by the slow decay phase, is consistent with a flat power-law, $\nu F_\nu \approx \text{const}$. After ~ 300 s the X-ray light curve drops sharply.

A shock breakout through a thick wind is one of the leading models for this X-ray flash, due to its relatively long duration (Chevalier & Fransson 2008; Balberg & Loeb 2011; Svirski & Nakar 2014; Ioka, Levinson & Nakar 2019). According to this model the rising part of the light curve is produced during the shock breakout episode. The transition to a collisionless shock takes place near the peak and the shallow power-law originates from the propagation of the collisionless shock in the opti-

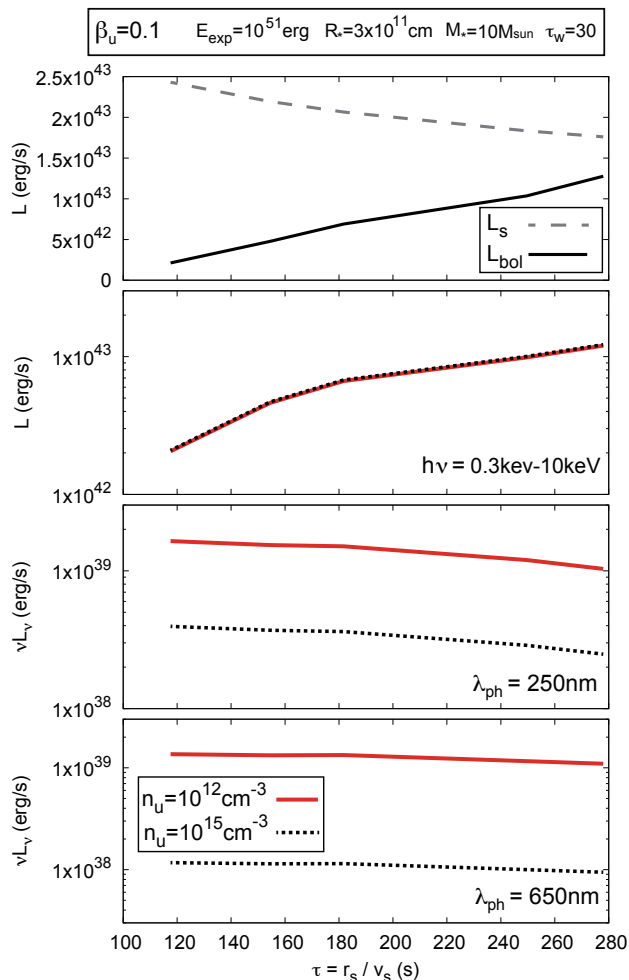


Figure 9. Estimated light curves based on the simulation results of $\beta_u = 0.1$. The assumed model parameters for the shock dynamics are $E_{exp} = 10^{51}$ erg, $R_* = 3 \times 10^{11}$ cm, $M_* = 10M_\odot$ and $\tau_w = 30$. In the top panel, the black solid line shows the bolometric luminosity. In addition, the shock luminosity is also displayed with grey dashed line for comparison. The lower panels display the luminosities at a given band: X-ray ($h\nu = 0.3 - 10$ keV), NUV ($\lambda_{ph} = 250$ nm) and optical ($\lambda_{ph} = 650$ nm). The dashed black lines are the results computed from the fiducial simulations which assume $n_u = 10^{15}$ cm $^{-3}$. The solid red lines are the light curves deduced for $n_u = 10^{12}$ cm $^{-3}$. Note that the bolometric light curve does not vary with the density n_u since the shock structure does not change.

cally thick wind (Svirski & Nakar 2014). The sharp decline after ~ 300 s marks the transition of the shock to the optically thin wind region. Previous studies examined this model based on the time and energy scales of the entire emission (Chevalier & Fransson 2008; Balberg & Loeb 2011), and based on a detailed comparison of the light curve and spectrum from the collisionless phase (post breakout) to a theoretical model (Svirski & Nakar 2014). With our current study we can examine the compatibility of the predicted spectrum and the total luminosity in the XRT energy window (0.3-10 keV) with the observations.

According to the modelling of the post-peak emission (Svirski & Nakar 2014) we find a breakout velocity of $\beta_u \approx 0.2-0.4$ and a breakout radius $R_{bo} \sim 10^{12}$ cm. Thus, the parameters adopted in figure 10 ($\beta_u = 0.25$, $n_u = 10^{12}$ cm $^{-3}$) are in agreement with those inferred for XRT 080109. The luminosity predicted for this choice

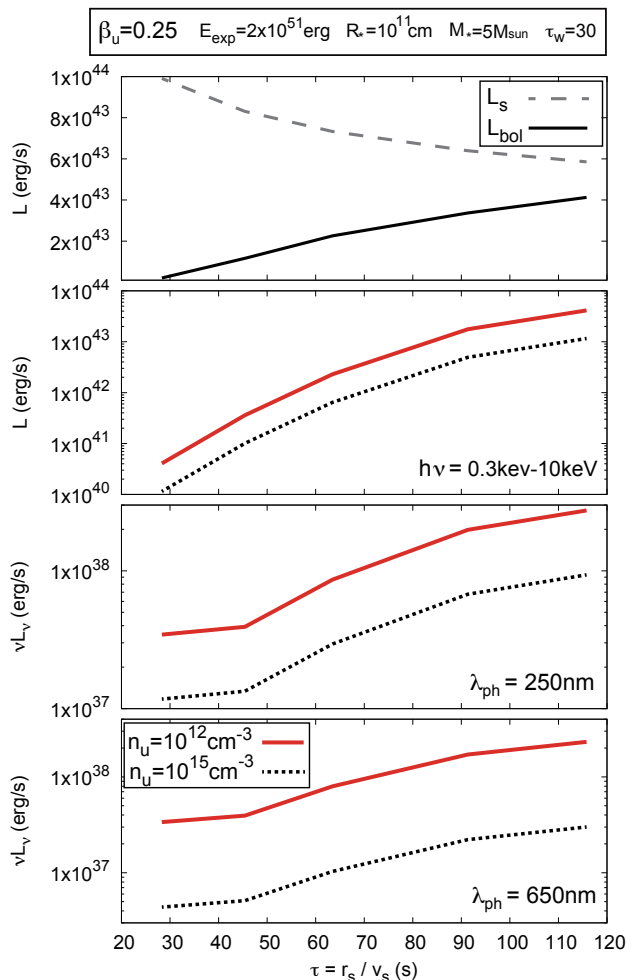


Figure 10. Same as Fig. 9, but for $\beta_u = 0.25$. The assumed model parameters for the shock dynamics are $E_{exp} = 2 \times 10^{51}$ erg, $R_* = 10^{11}$ cm, $M_* = 5M_\odot$ and $\tau_w = 30$.

of parameters in the XRT spectral window is in general agreement with the observations. The νF_ν spectrum, as shown in figures 7 & 8, peaks at early time (small value of f) around ~ 20 keV and at late times (near the peak) around ~ 5 keV. The peak of the integrated spectrum during the rising phase for $\beta_u = 0.25$ and $n_u = 10^{12}$ cm $^{-3}$ is ~ 10 keV. For a breakout velocity of $\beta_u = 0.2$ the peak of the integrated spectrum is smaller, ~ 5 keV. This implies that if XRT 080109 is a wind breakout then the rising phase is harder than the decay. This is compatible with the analysis of Soderberg et al. (2008) that find a significant spectral softening during the outburst. Moreover, while the spectrum during the decay phase is expected to be a power-law with $\nu F_\nu \approx \text{const}$ (Svirski & Nakar 2014b), the breakout spectrum near the peak of νF_ν is expected to deviate from a power-law. It may be possible to identify such deviation in a re-analysis of the rising phase of XRT 080109.

7 DETECTABILITY

The short duration of the shock breakout makes it very challenging for detection. One interesting property of shock breakout from a stellar wind is that for the anticipated range of conditions the bolometric luminosity emitted during the breakout phase is predicted to

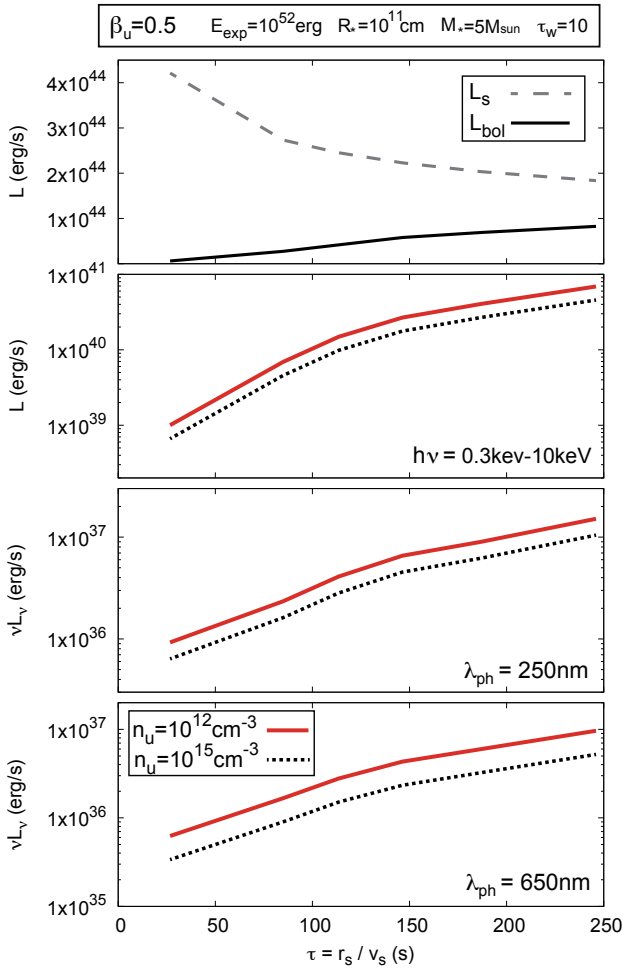


Figure 11. Same as Fig. 9, but for $\beta_u = 0.5$. The assumed model parameters for the shock dynamics are $E_{exp} = 10^{52}$ erg, $R_* = 10^{11}$ cm, $M_* = 5M_\odot$ and $\tau_w = 10$.

lie within a narrow range. It is almost independent of the progenitor radius and the wind opacity ($L \propto (R_* \tau_w)^{0.1}$), and its dependence on the explosion energy and the inverse of the ejecta mass is roughly linear. We estimate that for any progenitor type and any mass-loss history (prior to the explosion) the breakout luminosity is expected to fall in the range $L_s \sim 10^{43} - 10^{44}$ erg. Different progenitors and explosion conditions may be distinguished by the overall duration and total energy of the breakout pulse.

γ -rays: The spectral range at which the breakout luminosity is released depends on its velocity. For $\beta_u \approx 0.35 - 0.5$ most of the energy is released in soft γ -rays. The luminosity for these velocities is $\sim 10^{44}$ erg/s (figure 11), which makes them extremely hard to detect with current gamma-ray detectors. Even the Swift BAT, which is the most sensitive detector of soft gamma-rays currently in operation, can detect such flares only up to a distance of ~ 5 Mpc. It is therefore not surprising that shock breakouts from regular type Ib/c supernovae have not been detected in gamma-rays thus far.

X-rays: A bright signal in the spectral window of most X-ray detectors, 0.3-10 keV, is expected for breakout velocities $\beta_u \approx 0.1 - 0.35$. The range of luminosities in X-rays at these velocities is $\sim 1 - 5 \times 10^{43}$ erg/s (figures 9 and 10) and the duration

is ~ 50 s for canonical parameters, and longer for a very massive wind. The most promising instrument for detection of such signals is eROSITA. Its single-scan sensitivity is $\sim 10^{-13}$ erg s $^{-1}$ cm $^{-2}$ in the 0.5-10 keV band, and it scans the sky, spending ~ 40 s on each location within its 0.833 deg 2 field of view (Merloni et al. 2012). Thus, it can detect a shock breakout from a thick wind at a velocity of $\beta_u \approx 0.1 - 0.35$ up to a redshift of $z \approx 0.25$, which corresponds to a volume of ~ 5 Gpc 3 . Given that the rate of type Ib/c SNe is $\sim 2.5 \times 10^4$ Gpc $^{-3}$ yr $^{-1}$ (Li et al. 2011), and assuming that a shock breakout from a thick wind is common in this type of SNe (as suggested by the serendipitous detection of SN 2008D), we predict that eROSITA will detect roughly one SN shock breakout signal every year.

UV/optical: While the predicted UV and optical signals are much brighter than previously predicted, it is still rather faint. The brightest signal, expected for $\beta_u = 0.1$ in these bands, has a luminosity of $\sim 10^{39}$ erg/s (figure 9), which corresponds to an absolute AB magnitude $M \sim -9$. Given the rate of type Ib/c SNe, such signal is much too faint for detection by any of the current and near future optical/UV surveys.

8 SUMMARY AND CONCLUSIONS

We performed Monte-Carlo simulations of photon-starved RMS that incorporate the leakage of photons from the shock, for shock velocities $\beta_u = 0.1, 0.25$ (fast Newtonian regime) and $\beta_u = 0.5$ (mildly relativistic regime). We combined the simulation results with a shock propagation model to compute the signal emitted during a gradual shock breakout from a stellar wind. This is the first prediction of the breakout emission from a wind obtained from first principles calculations. The main conclusion is that the flux emitted at frequencies below the SED peak (particularly the optical/UV band) is much higher (by orders of magnitude) from that hitherto anticipated by naively invoking a Wien spectrum downstream of the shock. A detailed summary of the main results follows:

(i) We find that in the fast Newtonian RMS ($\beta_u = 0.1$ and 0.25) the temperature in the immediate downstream decreases with increasing radiative losses, in agreement with the prediction of the analytical model of Ioka, Levinson & Nakar (2019). This results from the enhancement of the photon density with increasing shock compression ratio (due to a slower photon diffusion downstream). As a consequence, the peak energy of the breakout emission ($E_p \sim 3kT \sim 1$ keV for $\beta_u = 0.1$ and ~ 10 keV for $\beta_u = 0.25$) shifts to lower values as the luminosity increases. This might give rise to a power-law feature in the time-integrated spectrum (as suggested in Fig. 7 for the $\beta_u = 0.25$ case) which could explain the spectrum of the shock breakout candidate XRT080109, as discussed in Ioka, Levinson & Nakar (2019). In contrast, in mildly relativistic shocks ($\beta_u = 0.5$) the temperature is regulated by pair creation and is, therefore, quite insensitive to the escape fraction. As a result, the peak energy of the emission is expected to be fixed during the breakout phase at around $E_p \sim 100$ keV. Our analysis predicts a detection rate of about one SN shock breakout event per year by eROSITA.

(ii) The time-resolved spectra of escaping photons are well described by a Wien spectrum at the energies around the SED peak and above. However, there is substantial softening of the portion of the spectrum below the peak ($f_\nu \propto \nu^{0-0.5}$) which extends down to the frequency below which free-free absorption becomes important. This implies that the soft emission should be much brighter

than the naive expectation assuming a Wien spectrum by orders of magnitude. Although it is not clear at present, the subshock found for $\beta_u = 0.5$ may give rise to efficient particle acceleration. In this case, the resulting spectrum may be affected by the accelerated pairs. Further investigation is necessary to pin down this issue.

(iii) The computed light curves show a gradual rise over tens to hundreds of seconds, depending on parameters, in all bands, except for the optical lightcurve of the $\beta_u = 0.1$ shock which is flat. The optical/UV luminosity is higher for slower shocks and lower breakout densities, as anticipated, and can reach 10^{40} ergs s⁻¹ for $\beta_u = 0.1$ at 250 nm. Unfortunately, this is still too low to be detected by current and near future optical/UV surveys.

(iv) The velocity profiles found for $\beta_u = 0.1$ and 0.25 are in good agreement with the analytical model of Ioka, Levinson & Nakar (2019). This result confirms that the diffusion limit provides a reasonable approximation for the radiation transfer at these velocities even when substantial energy is escaping from the shock. This is no longer true for the mildly relativistic shock $\beta_u = 0.5$. Contrary to the fast Newtonian shocks that exhibit a smooth shock profile for all escape fractions (at least up to $f_{esc} \sim 0.7$), in the $\beta_u = 0.5$ case a subshock forms when the losses exceed a certain value (a few percents) and then continues to grow as f_{esc} increases. In practice, this subshock can accelerate the pairs to nonthermal energies which, in turn, may lead to a non-thermal high-energy spectral component. Such a component was not included in our analysis. We plan to investigate the effect of the subshock on the evolution of the spectrum in a future work.

ACKNOWLEDGMENTS

This work was supported by JSPS KAKENHI Grant Number JP19K03878, JP19H00693 and JP20H04751. Numerical computations and data analysis were carried out on Hokusai BigWaterfall system at RIKEN, XC50 at Center for Computational Astrophysics, National Astronomical Observatory of Japan and the Yukawa Institute Computer Facility. This work was supported in part by a RIKEN Interdisciplinary Theoretical & Mathematical Science Program (iTHEMS) and a RIKEN pioneering project ‘‘Evolution of Matter in the Universe (r-EMU)’’ and ‘‘Extreme precisions to Explore fundamental physics with Exotic particles (E3-Project)’’. AL and EN acknowledge support by the Israel Science Foundation grant 1114/17.

REFERENCES

- Balberg, S., & Loeb, A. 2011, MNRAS, 414, 1715
 Blandford R. D., Payne D. G., 1981b, MNRAS, 194, 1041
 Campana, S., Mangano, V., Blustin, A. J., et al. 2006, Nature, 442, 1008
 Chevalier R. A., Fransson C., 2008, ApJL683, L135
 Chevalier R. A., Irwin C. M., 2011, ApJL, 729, L6
 Chevalier R. A., Irwin C. M., 2012, ApJL, 747, L17
 Gal-Yam, A., Arcavi, I., Ofek, E. O., et al. 2014, Nature, 509, 471
 Granot A., Nakar E., Levinson A., 2018, MNRAS, 476, 5453
 Ioka K., Levinson A., Nakar E., 2019, MNRAS, 484, 3502
 Ito H., Levinson A., Nagataki S., 2020, MNRAS, 492, 1902 (ILN20)
 Ito H., Levinson A., Stern B. E., Nagataki S., 2018, MNRAS, 474, 2828
 Katz B., Budnik R., Waxman E., 2010, ApJ, 716, 781
 Levinson A., Nakar E., 2020, Phys. Rep., 866, 1-46
 Li W., Chornock R., Leaman J., Filippenko A. V., Poznanski D., Wang X., Ganeshalingam M., Mannucci F., 2011, MNRAS412, 1473
 Merloni A., et al., 2012, arXiv e-prints, p. arXiv:1209.3114
 Modjaz, M., Li, W., Butler, N., et al. 2009, ApJ, 702, 226

- Nakar, E. 2015, ApJ, 807, 172
 Nakar E., Sari R., 2010, ApJ, 725, 904
 Ofek, E. O., Arcavi, I., Tal, D., et al. 2014a, ApJ, 788, 154
 Ofek, E. O., Rabinak, I., Neill, J. D., et al. 2010, ApJ, 724, 1396
 Ofek, E. O., Sullivan, M., Shaviv, N. J., et al. 2014b, ApJ, 789, 104
 Sakurai A., 1960, Comm. Pure Appl. Math., 13, 353
 Shiode, J. H., & Quataert, E. 2014, ApJ, 780, 96
 Soderberg A. M., et al., 2008, Natur, 453, 469
 Suzuki A., Shigeyama T., 2010, ApJ, 719, 881
 Svirski, G., & Nakar, E. 2014, ApJL, 788, L14
 Svirski G., Nakar E., 2014b, ApJ, 788, 113
 Svirski G., Nakar E., Sari R., 2012, ApJ, 759, 108
 Wang X.-Y., Li Z., Waxman E., Mészáros P., 2007, ApJ, 664, 1026
 Waxman, E., Mészáros, P., & Campana, S. 2007, ApJ, 667, 351
 Weaver T. A., 1976, ApJS, 32, 233

DATA AVAILABILITY

The data underlying this article will be shared on reasonable request to the corresponding author.